

Effect of Al content on hydrogen behavior of Ti-Al binary alloy

Hanbo Weng ^{a,b}, Qian Wang ^{b,*}, Linzhi Han ^b, Yandi Jia ^{a,b}, Shuo Cao ^b, Yingjie Ma ^{a,b,c,*}, Daokui Xu ^{d,*}, Sensen Huang ^b, Min Qi ^b, Qingmiao Hu ^b , Jianke Qiu ^{a,b}, Jiafeng Lei ^{a,b}, Rui Yang ^{a,b,c}

^a School of Materials Science and Engineering, University of Science and Technology of China, Shenyang 110016, China

^b Shi-changxu Innovation Center for Advanced Materials, Institute of Metal Research, Chinese Academy of Sciences, Shenyang 110016, China

^c Shenyang National Laboratory for Materials Science, Institute of Metal Research, Chinese Academy of Sciences, Wenhua Road 72, 110016 Shenyang, China

^d Key Laboratory of Nuclear Materials and Safety Assessment, Institute of Metal Research, Chinese Academy of Sciences, Shenyang 110016, China

ARTICLE INFO

Keywords:

Ti-Al binary alloy
Hydride
Hydrogen-induced cracking

ABSTRACT

This study systematically explores hydrogen behavior in Ti-xAl alloys ($x = 2, 4, 6, 8$ wt%). Specifically, the absorption capacity and diffusion rate are evaluated using hydrogen storage experiments. Thermal gas-phase hydrogenation experiments are conducted, and the hydride precipitation at different scales is characterized. First-principles calculations are performed to analyze H occupancy stability and the interactions between Al and H atoms. The experiment results demonstrate that the addition of Al reduces hydrogen absorption capacity and diffusion rate in Ti-xAl alloys. The strong attraction of Al to the H atom in octahedral interstitial site hinders the formation of Ti-H bonds, thereby suppressing the hydride nucleation. With increasing hydrogen concentration, the dominant orientation relationship (OR) shifts from OR2 ($\{0001\}\alpha/\{001\}TiH_x, <2\bar{1}\bar{1}0>\alpha/<011>TiH_x$) to OR1 ($\{0001\}\alpha/\{002\}TiH_x, <2\bar{1}\bar{1}0>\alpha/<011>TiH_x$). At lower hydrogen content (≈ 0.01 wt%), the hydride nucleation is accompanied by amount of $\{111\}$ stacking faults and twins. With the increased Al content, OR1 hydride is more favorable. Above 0.5 wt% H, all the hydrides exhibit OR1 with α -Ti. Meanwhile, the variant with minimum deviation from the hydride interface and grain boundary is preferably selected. Elevated Al content diminishes strain accommodation capacity while promoting hydrogen-induced crack initiation and modifying crack propagation behavior.

1. Introduction

Titanium alloys are widely utilized in aerospace, automotive, and military applications due to their exceptional strength-to-weight ratio, corrosion resistance, and high-temperature performance [1–3]. In aforementioned applications, titanium alloy components are frequently exposed to hydrogen-rich environments, including liquid fuel combustion processes and deep-ocean hyperbaric corrosion scenarios [4,5]. Direct exposure of titanium alloys to hydrogen-rich environments promotes rapid hydrogen absorption [6]. This phenomenon induces solid-solution strengthening and hydride precipitation in titanium alloys, directly compromising mechanical properties and long-term service stability [7,8]. Hence, the characteristic behavior induced by hydrogen in titanium alloys remains an imperative research priority.

The types and concentrations of alloying elements can significantly influence the hydrogen absorption and diffusion behavior.

Consequently, numerous explorations have been conducted from traditional steels to advanced alloys. In traditional steels, alloying elements such as Cr, Mo, Cu, and Ni significantly modify hydrogen absorption and diffusion through trap-site formation and electrochemical modulation mechanisms [9,10]. Further investigations reveal that Cu-substituted Ni induces reduced austenite stability and facilitates strain-induced martensite formation in steel to enhance hydrogen absorption and diffusion [11]. For medium-entropy alloys, Mo element impedes the hydrogen diffusion toward the grain boundaries by modifying deformation mechanisms [12]. In titanium alloys, β -stabilizers such as Fe and Cr promote hydrogen absorption and diffusion by increasing β -phase content [13]. The addition of Mo elevates hydrogen solubility, thereby modifying both hydrogen absorption and diffusion in titanium alloys [14]. Beyond the aforementioned elements, the α -phase stabilizer Al demonstrates remarkable corrosion resistance in titanium alloys [15]. However, the hydrogen absorption and diffusion mechanism mediated

* Corresponding authors.

E-mail addresses: wangqian@imr.ac.cn (Q. Wang), yjma@imr.ac.cn (Y. Ma), dkxu@imr.ac.cn (D. Xu).

Table 1
Chemical analysis of Ti-xAl forged bars.

Alloys	Element Concentration wt%	
	Al	H
Ti-2Al	2.09	0.0016
Ti-4Al	3.84	0.0026
Ti-6Al	6.02	0.0048
Ti-8Al	7.75	0.0034

by Al in titanium alloys remains incompletely elucidated.

In addition to the effect of absorption and diffusion, the mechanism of hydride precipitation in titanium alloys is recognized as critically important. The precipitated hydrides in titanium alloys are primarily classified into γ , ϵ , and δ hydrides. Both γ and ϵ hydrides possess a face-centered tetragonal structure (FCT) with chemical compositions of TiH and TiH_x ($1.8 < x \leq 2$), respectively [7]. In contrast, δ hydrides have a face-centered cubic structure (FCC) with composition TiH_x ($1.5 \leq x < 1.99$) [16,17]. Hydride precipitation is dictated by distinct microstructural control parameters [18]. Conforto et al. [19] established the correlation between hydrogen concentration and hydride types. Wang et al. [20] discovered that grain orientation controls δ -hydride orientations in α -Ti through anisotropic strain accommodation. Long et al. [21] identified temperature-cooling rate dependence in hydride phase selection by acquiring various metastable γ' -hydride fractions at different-temperature water quenching. As an α -stabilizing element, Al inevitably influences the precipitation types of hydrides in titanium alloy. Nevertheless, the specific effect of Al on hydride transition in titanium alloys remains unresolved.

Hydrogen and hydride accumulation elevates hydrogen-induced cracking susceptibility [22,23]. Dissolved hydrogen induces lattice expansion and local stress concentration in the matrix leading to microcrack nucleation. Surface cracks dominate the α phase, while internal cracks prefer α/β interfaces [24]. During propagation, cracks preferentially extend along α/β phase interfaces [22,25–27]. Notably, some cracks can overcome phase boundary barriers and propagate along slip planes due to the Burgers orientation relationship between α/β phases [28]. Hydride morphology also plays a critical role in hydrogen-induced cracking. Thin hydrides (less than 400 nm) deform cooperatively with the matrix through interfacial dislocation transfer whereas thick hydrides tend to fracture under high stress due to blocked dislocation channels [29]. Deformation mechanisms further regulate crack behavior. Slip bands retard crack growth while twinning shear promotes hydride fracture [10]. Al alloying modifies the matrix strength and deformation mode thereby altering hydrogen-dislocation interactions. However, its specific effects on hydrogen-induced cracking require further investigation.

Table 2
Chemical analysis of Ti-xAl powder.

Alloys	Element concentration wt%		
	Al	H	O
Ti-2Al	2.01	0.0023	0.056
Ti-4Al	3.92	0.0026	0.067
Ti-6Al	5.98	0.0027	0.059

In this work, the effect of Al content on the hydrogen behavior of Ti-xAl ($x = 2, 4, 6, 8$ wt%) binary alloy was studied by thermal gas-phase hydrogenation. Key aspects such as hydrogen absorption, diffusion, and hydride formation were analyzed. The role of Al in hydride formation was further validated through the estimation of volume distortion and first-principles calculation. Additionally, the impact of Al on hydride variant selection was explored based on electron backscatter diffraction (EBSD) and transmission electron microscope (TEM). Finally, the hydrogen-induced cracking behaviors in Ti-xAl alloys were investigated.

2. Experimental procedure and theoretical calculations

2.1. Material preparation

Ti-xAl forged bars used in this study were prepared through three times vacuum arc remelting, followed by successive deformations in β and $\alpha + \beta$ phase fields. The chemical composition analysis of the as-received Ti-xAl ($x = 2, 4, 6, 8$ wt%) alloys is depicted in Table 1. The Ti-xAl alloys were subjected to homogenization treatment at 970 °C, 1020 °C, 1070 °C, and 1100 °C (50 °C above the β transus temperature) for 1 h, followed by furnace cooling. Scanning Electron Microscope (SEM) and Backscattered Electron (BSE) observations were conducted by Tescan MIRA3 SEM. BSE images of Ti-xAl alloys after homogenization treatment are presented in Fig. 1a-d. The uniform α lamella grain boundaries (GBs) are mainly observed in the Ti-xAl alloys. X-ray diffraction (XRD) experiments were performed by Bruker D8 Discover X-ray diffractometer with high-energy ($\lambda = 1.54056$ Å) X-ray illumination. Fig. 1e shows the XRD spectrum of homogenized Ti-xAl ($x = 2, 4, 6, 8$ wt %) alloys. The XRD spectrum only shows peaks from the α -Ti matrix, with no β phase detected. As the Al content rises, a slight increase in the diffraction angle corresponds to the increased lattice distortion of the α phase.

To analyze the effect of Al on hydrogen diffusion and absorption in titanium alloys, hydrogen storage experiments were conducted. Ti-2Al, Ti-4Al, and Ti-6Al powder (1 g each with a particle size of 25 μm) was prepared. The chemical composition of Ti-xAl powder is shown in Table 2. Hydrogen absorption kinetics experiments were conducted using an automatic pressure-composition-temperature (PCT) hydrogen

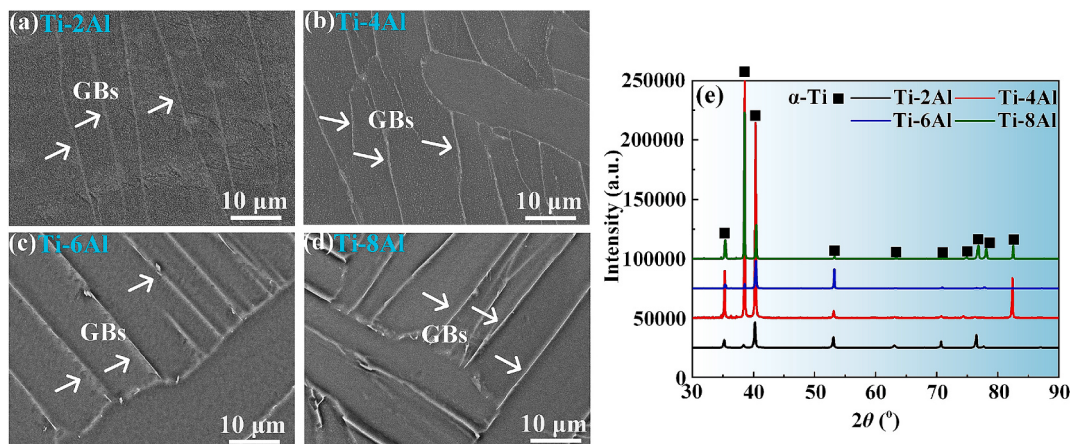


Fig. 1. BSE microstructure after homogenization treatment of (a) Ti-2Al, (b) Ti-4Al, (c) Ti-6Al, and (d) Ti-8Al alloys; (e) X-ray spectra of Ti-xAl alloys.

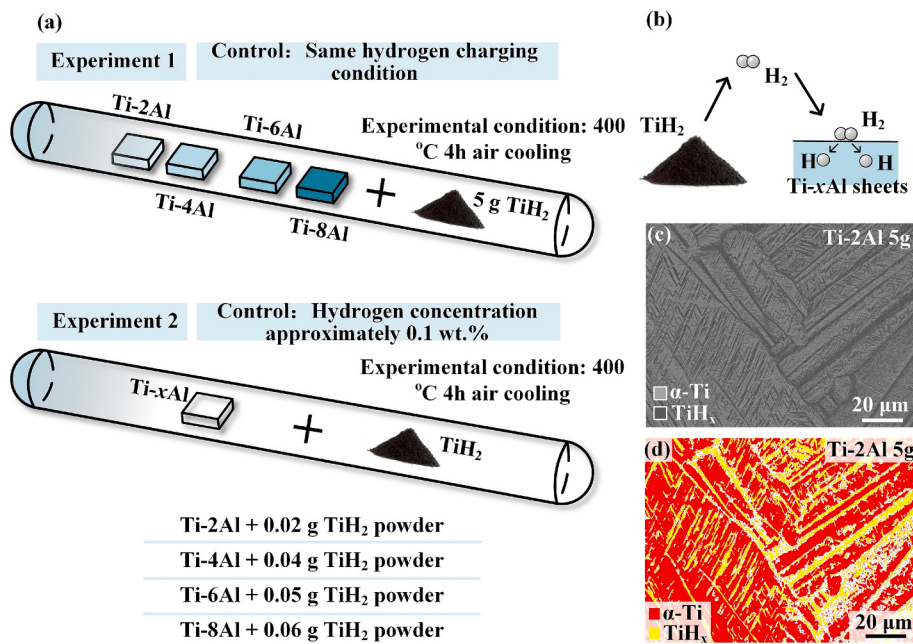


Fig. 2. (a) Experimental diagram for thermal gas-phase hydrogenation; (b) Process of H entering the alloy sheet from TiH₂ powder; (c) BSE and (d) EBSD schematic diagrams of α-Ti and TiH_x morphology after thermal gas-phase hydrogenation.

storage tester (H2PCT-1101). The testing pressure and temperature were set at 3 MPa and 400 °C.

2.2. Thermal gas-phase hydrogenation

Hydrogen diffusion in α-Ti is uneven at room temperature. Thus, hydrogenation was carried out at elevated temperatures. Ti-xAl samples with a size of 10 × 10 × 3 mm were wet-ground with SiC papers down to 800 grit before hydrogen charging. Each sheet of Ti-xAl alloys and the TiH₂ powder was sealed in the vacuum glass tube. The outer diameter of the vacuum glass tube is 16 mm; the inner diameter is 13 mm, and the length is 130 mm. Fig. 2a outlines the experimental setup. Two sets of experiments were designed. Experiment 1: Ti-xAl sheets were sealed in the same tube and hydrogen-charged with 5 g of TiH₂ powder. Experiment 2: To obtain the same hydrogen concentration in each Ti-xAl sheet, the samples were charged with different amounts of TiH₂. The Ti-2Al, Ti-4Al, Ti-6Al, and Ti-8Al alloys corresponded to 0.02 g, 0.04 g, 0.05 g, and 0.06 g of TiH₂ powder, respectively. 4 h holding at 400 °C was applied to all tubes to ensure uniform distribution of soluble hydrogen atoms. Hydrogen concentration is primarily controlled by the mass of TiH₂ powder. Increasing the TiH₂ powder liberates more H₂, thereby raising the pressure within the vacuum tube and increasing the hydrogen uptake by the alloy sheets. The hydrogen concentration in the charged samples was measured using an ONH 836 oxygen/nitrogen/hydrogen elemental analyzer. The process of H₂ transfer from TiH₂ powder to the alloy sheet is illustrated in Fig. 2b. Initially, TiH₂ powder decomposes into H₂ at 400 °C. H₂ comes into contact with the alloy sheet and dissociates into H atoms, which then dissolve into the alloy. When the concentration of H atoms exceeds the critical level in α-Ti, hydrides precipitate.

After hydrogen charging, the Ti-xAl ($x = 2, 4, 6, 8$ wt%) sheets were ground with SiC paper up to 2000 grit. The surfaces were then manually polished using a SiC slurry to achieve a mirror-like finish. Vibratory polishing was performed to eliminate residual stresses on the surface. EBSD analysis was conducted using a Tescan MIRA3 SEM equipped with an EDAX Hikari EBSD camera. The TEM specimen was first mechanically ground to approximately 50 μm, followed by electropolishing using a solution of 5 vol% HClO₄, 35 vol% C₄H₁₀O, and 60 vol% CH₃OH. The electropolishing was performed under conditions of −25 °C to −18 °C

and 20 V. The hydrides were observed using bright-field TEM and high-resolution TEM on an FEI Talos F200X operated at 200 kV.

The BSE morphology of the Ti-2Al alloy sample after hydrogen charging with 5 g of TiH₂ was selected as a schematic representation of the hydride morphology (see Fig. 2c). The light gray regions represent the α-Ti matrix, while the dark gray regions represent the hydrides. The corresponding EBSD analysis is shown in Fig. 2d, where the red and yellow phases represent the α-Ti matrix and hydrides, respectively. The zero solutions may result from significant lattice distortion caused by hydrogen diffusion or hydride formation. It can be observed that the morphology of hydrides precipitated at the GBs of the alloy is relatively wide. In contrast, the hydrides within the α grains exhibit a short rod-like shape, arranged either in parallel or in a cross pattern.

2.3. First-principles calculation

The relationship among Al atoms, H atoms, and hydrides in titanium alloys was analyzed using first-principles calculations. The calculations were performed using the Vienna Ab-initio Simulation Package (VASP), based on the first-principles plane-wave pseudopotential method [30,31]. The electronic exchange–correlation functional was described using the Generalized Gradient Approximation (GGA) parameterized by the Perdew-Burke-Ernzerhof (PBE) scheme [32]. The interaction between electrons and atomic nuclei was represented by the Projector Augmented Wave (PAW) pseudopotentials. A plane-wave cutoff energy of 500 eV was used. The convergence criterion for electronic minimization was set to 1×10^{-6} eV/atom. For geometry optimization, the Hellmann-Feynman force tolerance was set to 1×10^{-3} eV/Å, and a k-point mesh of $4 \times 4 \times 3$ was employed. The energies of α-Ti and α-Ti with a single Al atom were used as reference states to investigate the solution and interaction energies of H atoms in Ti-xAl alloy. The α-Ti cell is multiplied by $4 \times 4 \times 3$ to create the corresponding pure Ti supercell, which contains 96 atoms. The H atom is initially placed in two distinct interstitial sites within the pure Ti lattice: the tetrahedral interstices (T sites) and the octahedral interstices (O sites). A single Al atom is randomly inserted into the Ti lattice. The H atom is then positioned in tetrahedral and octahedral interstices near the Al atom to explore local structural and energetic effects. Specifically, for the tetrahedral sites, the H atom is placed at the nearest-neighbor position (T1) and the next-

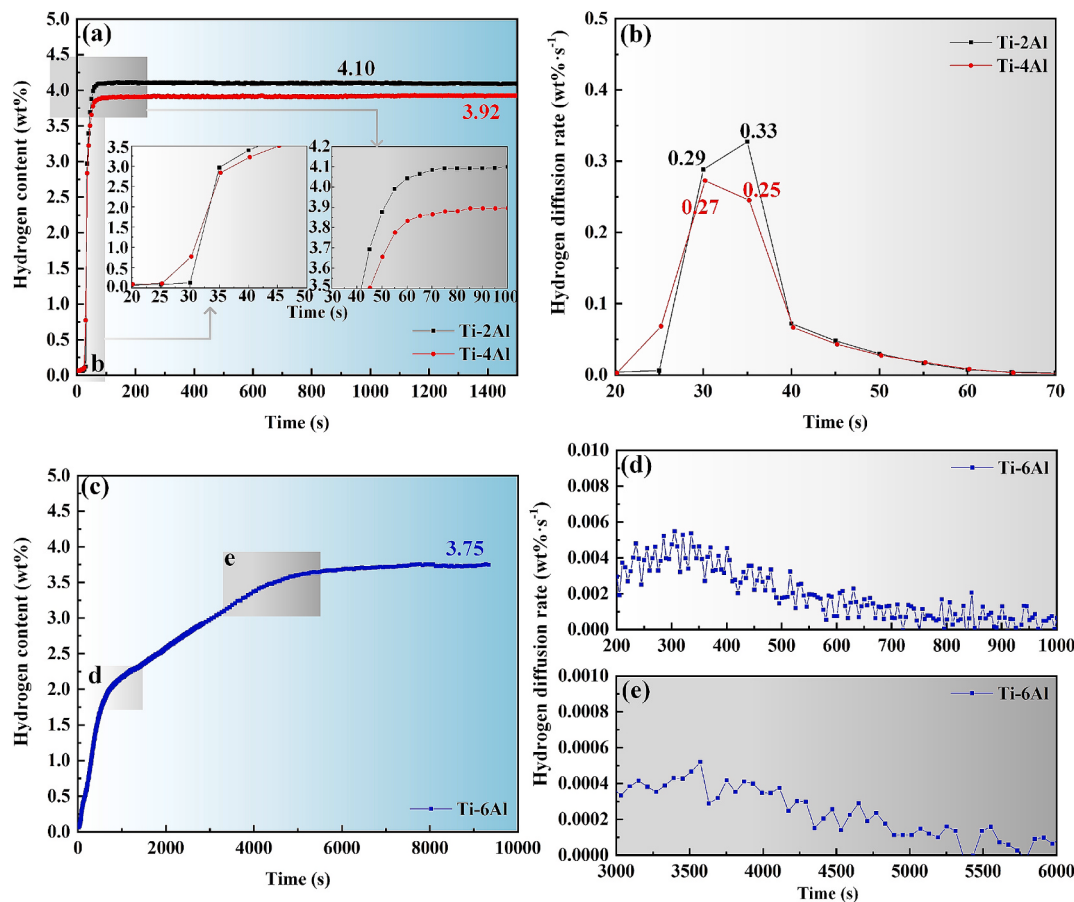


Fig. 3. (a) Hydrogen absorption kinetics curves of Ti-2Al and Ti-4Al alloys and (b) the corresponding hydrogen diffusion rate curves; (c) Hydrogen absorption kinetics curve of the Ti-6Al alloy and (d), (e) the corresponding hydrogen diffusion rate curve. (The experiments were conducted at a temperature of 400 °C and a hydrogen pressure of 3 MPa.).

nearest neighbor position (T2) relative to the Al atom. Similarly, for the octahedral sites, the H atom is placed at the nearest-neighbor position (O1) and the next-nearest-neighbor position (O2). The stable occupancy of solute H in the alloy is determined by comparing the solution energy and interaction energy of H atoms at different sites. A lower solution energy corresponds to a more stable occupancy state. The solution energy of a hydrogen atom is defined as:

$$E_{sol} = E_{M+H} - E_M - \frac{1}{2}E_{H_2} \quad (1)$$

where E_{M+H} and E_M represent the total energies of the bulk system with and without H, respectively. E_{H_2} denotes the total energy of the hydrogen molecule, which is calculated in a vacuum box with dimensions of 15 Å × 15 Å × 15 Å. The result is -6.76 eV. The interaction energy of H with the bulk alloy model containing alloy atoms is given by:

$$E_{inter} = E_{Ti+Al+H} + E_{Ti} - E_{Ti+Al} - E_{Ti+H} \quad (2)$$

where $E_{Ti+Al+H}$ represents the energy of the Ti bulk system containing one Al atom and one dissolved H atom, E_{Ti} denotes the energy of the α-Ti bulk system, E_{Ti+Al} represents the energy of the bulk system with one Al atom inserted, and E_{Ti+H} denotes the energy of the pure Ti bulk system with one dissolved H atom.

The free energy of the system at finite temperature is expressed as:

$$G = E_0 - TS + F_{vib}(T) \quad (3)$$

where E_0 is the total energy at 0 K, which can be directly obtained from first-principles calculations. S represents the configurational entropy. In elemental crystals and ordered solid solutions, the configurational

entropy can be neglected due to the fully ordered structure. $F_{vib}(T)$ is the vibrational free energy, which can be calculated from the ω_i as follows:

$$F_{vib}(T) = \sum_i^{3N} \frac{\hbar\omega_i}{2} + \sum_i^{3N} kT \ln \left(1 - e^{-\frac{\hbar\omega_i}{kT}} \right) \quad (4)$$

where \hbar is the reduced Planck constant, and k_B is the Boltzmann constant. The vibrational frequencies ω_i can be extracted from the force constant matrix calculated using the finite displacement method within first-principles calculations. In this work, the zero-point vibrational energy (ZPE) of the Ti-Al-H system, which corresponds to the first term on the right-hand side of Equation (4), has been evaluated. The hydrogen atoms are expected to contribute the dominant portion of the ZPE due to their small mass. To reduce the computational cost, only the vibrational frequencies of hydrogen atoms were considered. Specifically, when calculating the force constant matrix, only hydrogen atoms were allowed to move, while Ti and Al atoms were held fixed.

3. Results

3.1. Effect of Al on hydrogen absorption and hydride transformation

3.1.1. Hydrogen absorption kinetics

The hydrogen absorption capacity of Ti-xAl alloys was evaluated to assess their hydrogenation kinetics. Fig. 3 illustrates the variation in hydrogen absorption and diffusion of Ti-xAl alloys over time. Experiments were conducted at 400 °C with an initial hydrogen pressure of 3 MPa. The maximum hydrogen absorption was 4.10 wt% and 3.92 wt% for Ti-2Al and Ti-4Al alloys, respectively (Fig. 3a), while the Ti-6Al alloy

Experiment 1:

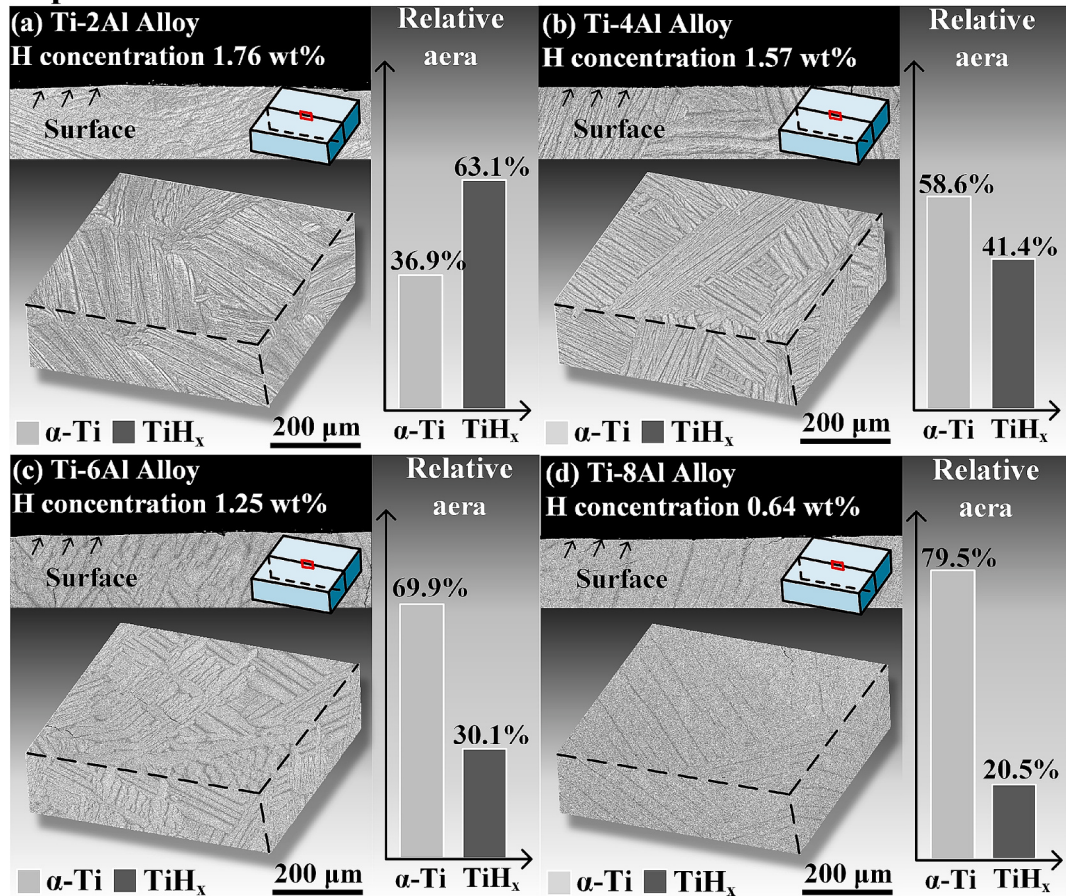


Fig. 4. BSE hydride morphologies of Ti-xAl ($x = 2, 4, 6, 8$ wt%) alloys after hydrogen charging: (a) Ti-2Al, (b) Ti-4Al, (c) Ti-6Al, and (d) Ti-8Al.

absorbed 3.75 wt% (Fig. 3c). Studies have demonstrated that the incorporation of Al destabilizes the hydrides in refractory high-entropy alloys thermodynamically, thereby reducing their hydrogen storage capacity [33]. It can be inferred that the inhibitory effect of Al on the hydrogen absorption capacity of titanium alloys follows a similar mechanism.

The hydrogen absorption curves indicate that the hydrogen absorption rates (or hydrogen diffusion rates) of Ti-2Al and Ti-4Al are similar (Fig. 3a). By differentiating the curves, the relationship between diffusion rates and time was obtained, as shown in Fig. 3b. It was observed that there are slight differences in their diffusion rates. At 30 s, the hydrogen diffusion rate of the Ti-2Al alloy reached $0.29 \text{ wt\%}\cdot\text{s}^{-1}$, while that of the Ti-4Al alloy reached $0.27 \text{ wt\%}\cdot\text{s}^{-1}$. At 35 s, the hydrogen diffusion rate for the Ti-2Al alloy increased to $0.33 \text{ wt\%}\cdot\text{s}^{-1}$, whereas the Ti-4Al alloy reached only $0.25 \text{ wt\%}\cdot\text{s}^{-1}$. Thus, a small amount of Al can slightly reduce the hydrogen diffusion rate in titanium alloys.

The hydrogen absorption curve of the Ti-6Al alloy was analyzed. In regions d and e of Fig. 3c, the hydrogen absorption rate significantly decreases. The relationship between diffusion rates and time is shown in Fig. 3d and e. The maximum hydrogen diffusion rate of the Ti-6Al alloy is around $0.0055 \text{ wt\%}\cdot\text{s}^{-1}$ at 305 s as shown in Fig. 3d. The Ti-2Al and Ti-4Al alloys require approximately 60 s to become fully hydrogenated, whereas the Ti-6Al alloy requires about 6000 s (Fig. 3c and e).

3.1.2. Microstructure characterization after thermal hydrogenation

Ti-xAl sheets were hydrogen charging together with 5 g of TiH_2 powder (Experiment 1 in Fig. 2a). Fig. 4 shows the hydrogen concentration and BSE morphology of Ti-xAl ($x = 2, 4, 6, 8$ wt%) alloys after hydrogen charging. The internal morphology and surface morphology

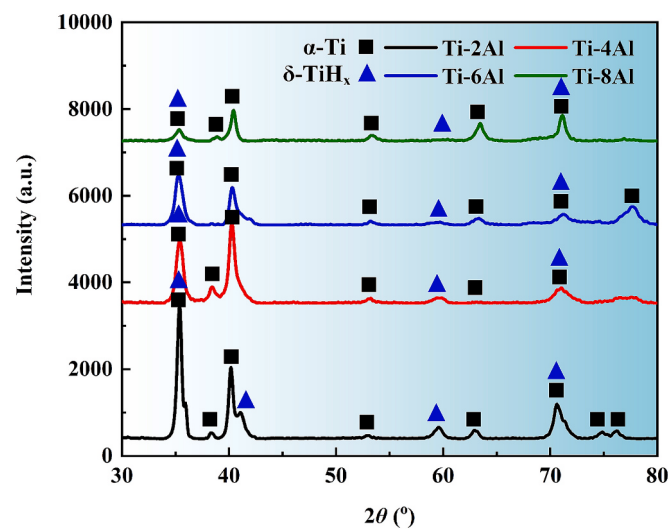


Fig. 5. X-ray spectra of Ti-xAl alloys after hydrogen charging.

indicate that the distribution of hydrides is uniformly dispersed within the samples. The hydrogen concentrations are 1.76 wt% (Ti-2Al), 1.57 wt% (Ti-4Al), 1.25 wt% (Ti-6Al), and 0.64 wt% (Ti-8Al). This demonstrates that as the Al content increases, the hydrogen concentration progressively decreases. Thus, the presence of Al impedes the absorption of H into the samples. This is consistent with the results presented in Section 3.1.1. In the Ti-2Al alloy (Fig. 4a), the morphology of hydrides is

Experiment 2:

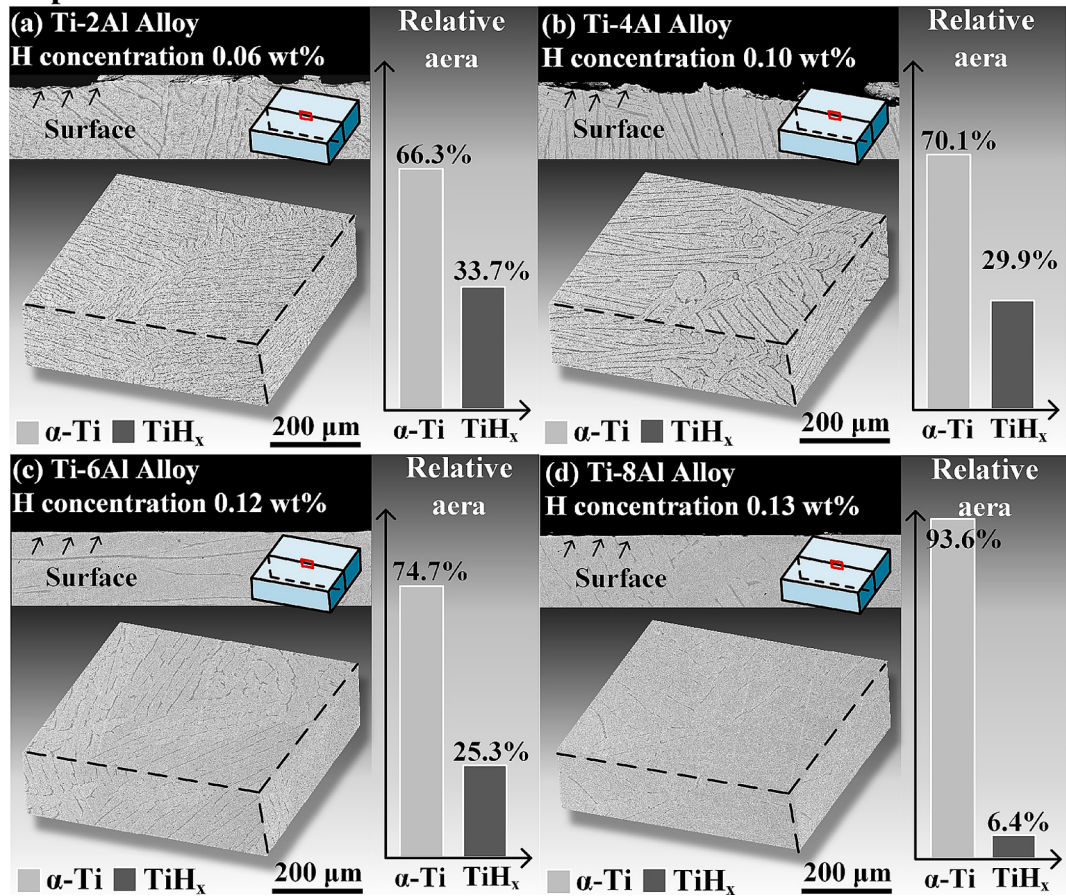


Fig. 6. BSE hydride morphologies of Ti-xAl ($x = 2, 4, 6, 8$ wt%) alloys under different hydrogen charging conditions: (a) Ti-2Al, (b) Ti-4Al, (c) Ti-6Al, and (d) Ti-8Al.

predominantly lamellar at GBs, with fine hydrides within α grains. As the Al content increases to 4 wt%, as shown in Fig. 4b, the fine hydrides within the grains decrease. In the Ti-6Al and Ti-8Al alloys (Fig. 4c and d), the fine hydrides are absent. The lamellar hydrides at GBs in the Ti-8Al alloy are finer and the hydrides exhibit a discontinuous distribution. In general, hydrides preferentially nucleate at grain boundaries and then precipitate within the grains.

Fig. 5 shows the XRD patterns of Ti-xAl alloys after hydrogen charging. The predominant hydride present in the alloy is δ -TiH_x, which exhibits a face-centered cubic (FCC) structure with a lattice parameter of $a = 4.4 \text{ \AA}$. The peak corresponding to δ -TiH_x at 35° is the same as that of α -Ti. The peak at 59° decreases with increasing Al content, indicating a gradual reduction in the amount of hydride.

Additional experiments (Experiment 2 in Fig. 2a) were conducted to investigate the influence of Al on hydrides under the same hydrogen concentrations. The hydrogen concentrations were approximately 0.06 wt% in Ti-2Al, 0.10 wt% in Ti-4Al, 0.12 wt% in Ti-6Al, and 0.13 wt% in Ti-8Al alloys. Fig. 6 shows the BSE hydride morphologies in Ti-xAl alloys. In the Ti-2Al alloy, both lamellar hydrides and fine hydrides are observed. With an increase in Al content, the fine hydrides disappear, and the lamellar hydrides gradually decrease. It can be seen that the content of hydrides in titanium alloys is inhibited by Al. When the hydrogen content is the same, an increase in Al content can inhibit the nucleation of hydride, and lead to an increase in hydrogen solubility.

According to the experiments above, the influence of Al content on hydrogen behavior mainly includes two aspects. Firstly, Al reduces the hydrogen absorption capacity of Ti-xAl alloys. Furthermore, when hydrogen diffuses into the samples, Al can also inhibit the hydride nucleation and thus improve the solid solubility of H. The underlying

mechanism will be further analyzed in Section 4.1 using first-principles calculation.

3.2. Effect of Al on hydride nucleation mechanism

The variant selection of hydrides in Experiment 1 is further discussed through EBSD analysis. Fig. 7 illustrates the orientation relationship (OR) between hydrides and the matrix in Ti-2Al and Ti-6Al alloys, as well as the variant selection between hydride traces and GBs. The hydrides are classified into two categories based on their precipitation locations: intragranular hydrides and intergranular hydrides. Moreover, there are two predominant ORs between the hydrides and α -Ti:

$$\text{OR1: } \{0001\}\alpha/\{/002\}\text{TiH}_x; <2\bar{1}0>\alpha//<011>\text{TiH}_x$$

$$\text{OR2: } \{0001\}\alpha/\{\bar{1}1\bar{1}\}\text{TiH}_x; <2\bar{1}0>\alpha//<011>\text{TiH}_x$$

The OR between hydrides and the matrix α phase in Ti-2Al alloy is depicted in Fig. 7c and g. The purple, pink, and blue phases represent the α -Ti grain, intragranular and intergranular hydrides, respectively. Both the intragranular and intergranular hydrides exhibit an OR1 relationship with the matrix. Fig. 7f and h illustrate the OR between hydrides and the matrix α grain in Ti-6Al alloy. Only intergranular hydrides were formed in the Ti-6Al sample. The green and red grains represent the α -Ti matrix and intergranular hydrides, respectively. It can be observed that the hydrides exhibit OR1 with α -Ti matrix.

Moreover, Fig. 7g and h also reveal that the hydride has a variant selection preference. According to the $\{10\bar{1}0\}\alpha/\{1\bar{1}0\}\text{TiH}_x$ interface, OR1 hydride can be divided into three variants [20]: V1 ($10\bar{1}0\alpha/\{1\bar{1}0\}\text{TiH}_x$), V2 ($01\bar{1}0\alpha/\{1\bar{1}0\}\text{TiH}_x$), and V3 ($\bar{1}100\alpha/\{1\bar{1}0\}\text{TiH}_x$). These three variants correspond to three interface traces. The variant with the smallest angle between its interface trace and the GB is more likely to

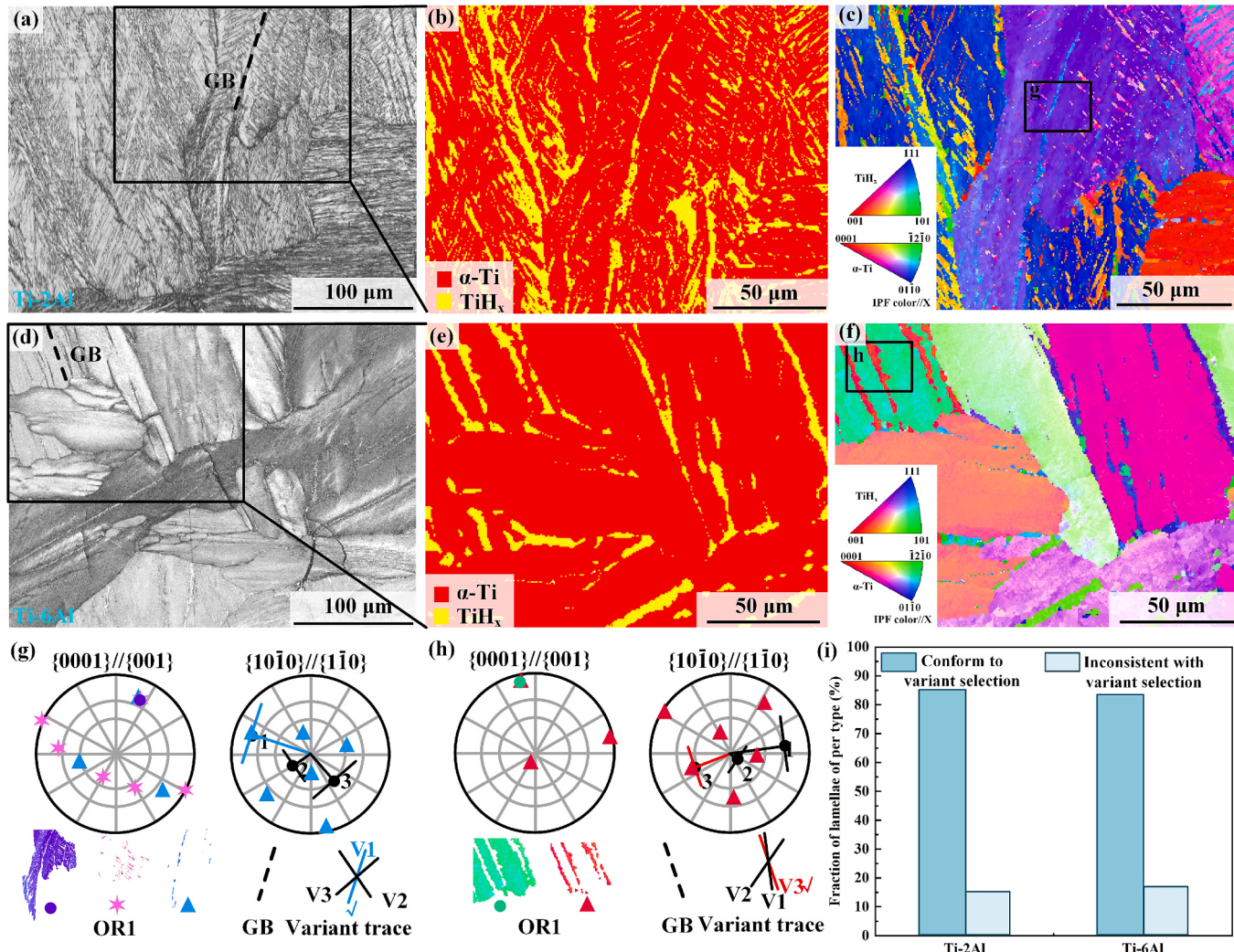


Fig. 7. (a) Band slope map, (b) phase map, and (c) IPF map of Ti-2Al alloy; (d) band slope map, (e) phase map, and (f) IPF map of Ti-6Al alloy; OR and variant selection of hydrides in (g) Ti-2Al and (h) Ti-6Al; (i) variant selection statistics for Ti-2Al and Ti-6Al alloys.

precipitate. In the Ti-2Al alloy, the variant of α -Ti and hydride is V1: $(10\bar{1}0)\alpha/(1\bar{1}0)TiH_x$, as shown in Fig. 7g. The V1 interface trace, indicated by the blue line, presents the minor angle with the GB direction (black dotted line). Thus, V1 is the preferred variant. Similarly, in Fig. 7h, V3 in the red line with a minimum deviation from the initial direction of the GB is also selected.

The hydride variants were statistically analyzed across different α colonies, with each colony counted as a single variant. The statistical data for both samples are illustrated in Fig. 7i. A total of 20 directions of GBs with precipitated hydride variants were investigated in the Ti-2Al alloy. The probability of the hydride conforming to the variant selection is 85 %. 12 GBs of the Ti-6Al were tested, of which 10 were suitable for variant selection and 2 were not. Consequently, the probability of variant selection in the Ti-6Al alloy is 83.3 %. Therefore, the Al content in Ti-xAl ($x = 2, 6$ wt%) alloys does not influence hydride variant selection at GBs.

The hydride size in Experiment 2 was insufficient for characterization via EBSD. Therefore, TEM experiments were conducted to analyze the hydride nucleation mechanism. Fig. 8 illustrates the TEM characterization of TiH_x hydrides in Ti-2Al, Ti-6Al, and Ti-8Al samples. In Ti-2Al alloy, hydride lamellae are predominantly present with an aspect ratio of approximately 10 (Fig. 8a). The corresponding diffraction pattern illustrates the OR between TiH_x and the α -Ti matrix as OR2. HRTEM images of the interface between the hydride and the α -Ti matrix

are displayed in Fig. 8b, demonstrating stacking faults at the interface. Fig. 8c and d present the TEM morphology of OR2 hydrides within the Ti-6Al alloy. The {111} twin spots were also observed inside the hydride. The orientation of the hydride twin is the same as that of the hydride matrix (OR2). Fig. 8d presents an HRTEM image of the hydride and hydride twin. Fig. 8e and f display the TEM morphology of the hydrogenated Ti-8Al alloy. In Fig. 8e, it can be discerned that the interior of the hydride is disordered. It is replete with a considerable amount of stacking faults. Additionally, a minute bone-like hydride is identified at the edge. The orientation between the hydride and the α -Ti matrix is OR1, which differs from the orientations of the hydrides observed in alloys with lower Al content. Fig. 8f depicts the hydride and α -Ti matrix interface through HRTEM images. It can be observed that {111} stacking faults are present within the hydride, and the angle of the atomic layers varies continuously. These results indicate that higher Al content increases the likelihood of stacking faults and lattice distortion within the hydrides.

To further analyze the bone-like hydrides in Ti-8Al alloy, a high-magnification analysis was conducted, as shown in Fig. 9a. The core of the hydride exhibits OR2 with the α -Ti matrix. The boundary of the hydride is characterized by numerous stacking faults (Fig. 9b), and the OR between the hydride boundary and the α -Ti matrix is closer to OR1 (Fig. 9c). This demonstrates the nucleation process of hydride twinning within the Ti-8Al. Fig. 9d shows the morphology of the hydride with a

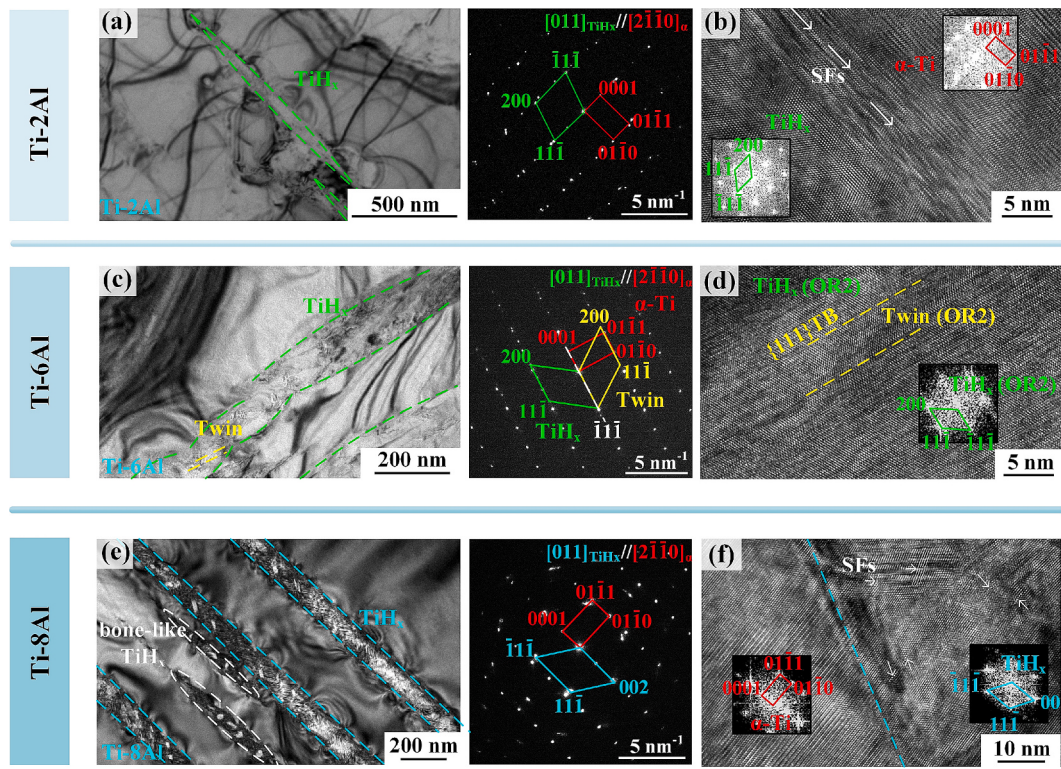


Fig. 8. TEM images of TiH_x, and the corresponding SAED patterns viewed along the $<011>$ TiH_x/ $<2\bar{1}\bar{1}0>$ α zonal axis of (a) Ti-2Al, (c) Ti-6Al, and (e) Ti-8Al. HRTEM images of TiH_x and the adjacent α -Ti matrix for (b) Ti-2Al, (d) Ti-6Al, and (f) Ti-8Al.

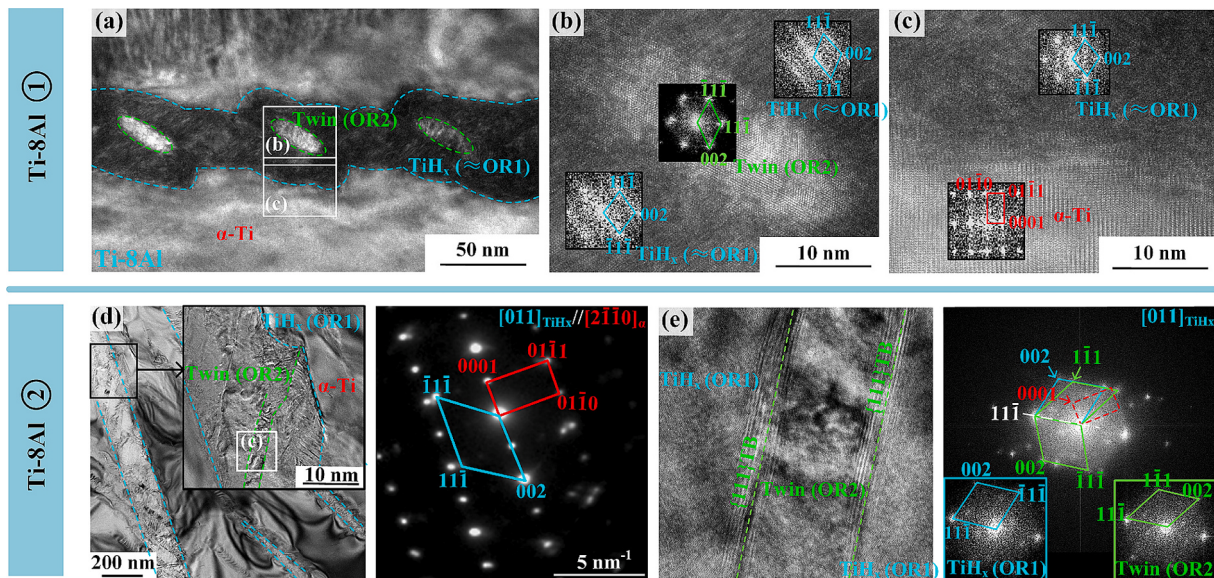


Fig. 9. (a) Morphology of a bone-like hydride in the Ti-8Al sample and corresponding HRTEM images of (b) the twin core and (c) the hydride interface; (d) TEM image of TiH_x in the Ti-8Al sample and the corresponding SAED pattern viewed along $<011>$ TiH_x/ $<2\bar{1}\bar{1}0>$ α zonal axis; (e) Amplified HRTEM images of the region marked by the white square in (d) and the corresponding FFT images.

growth twin. The hydride and twin follow OR1 and OR2 with the α -Ti matrix. The internal {111} twin of the hydride shown in Fig. 9d was further examined using HRTEM in Fig. 9e. According to the fast Fourier transform (FFT) image, the OR2 with an approximately 4° angular between the (1 $\bar{1}$ 1) plane of the hydride and the (0001) plane of the α -Ti matrix is consistent with previous studies [8]. Thus, the OR2 twin is primarily nucleated inside OR1 hydride, and can eventually extend through the entire lamella. In summary, at lower hydrogen content

(about 0.1 wt%), the hydride nucleation in Ti-2Al, Ti-4Al, and Ti-6Al alloys tends to follow OR2. As the Al content increases to 8 wt%, the hydride mainly follows OR1 with internal twins of OR2. At higher hydrogen contents (greater than 0.5 wt%), most of the hydrides exhibit OR1 with α -Ti matrix, as shown in Fig. 7. The reason for the change in OR will be further discussed in Section 4.2.

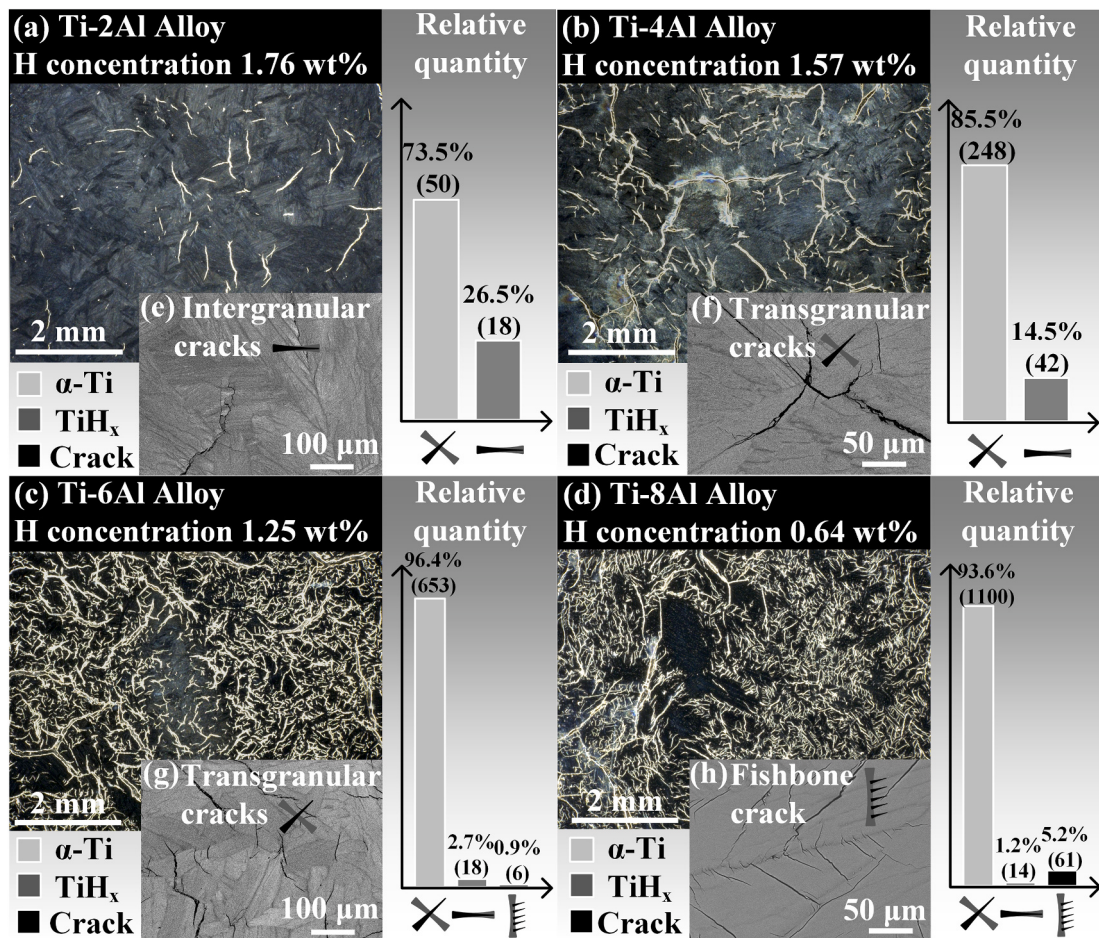


Fig. 10. Macroscopic and microscopic crack features with crack type statistics for (a) Ti-2Al, (b) Ti-4Al, (c) Ti-6Al, and (d) Ti-8Al alloys.

3.3. Effect of Al on hydrogen-induced cracking

Fig. 10a-d initially depicts the low-magnification morphology of cracks in Ti-xAl ($x = 2, 4, 6, 8$ wt%) alloys from Experiment 1. The crack-free regions in Fig. 4 were intentionally selected. With a $20 \times$ higher magnification than Fig. 10, hydride characterization in Fig. 4 could be performed in undisturbed zones, ensuring clear microstructural analysis. In the Ti-2Al alloy, only a small number of cracks were observed, while in the Ti-4Al alloy, the number of fine cracks increased, accompanied by the appearance of large cracks. In the Ti-6Al and Ti-8Al alloys, a significant reduction in crack size and an increase in crack density were observed. Fig. 10 illustrates the high-magnification morphology of cracks in Ti-xAl alloys. In Ti-2Al alloy (Fig. 10a), the cracks mainly propagate along the GBs because more hydrides are concentrated there. With Al content increasing, transgranular cracks are observed and increase significantly (Fig. 10b-d). Here, transgranular cracking is defined by fracture paths that cut directly through hydride, rather than following them. The hydrogen absorption and the precipitation of hydrides are accompanied by volume expansion [8,26]. The volume expansion of $\delta\text{-TiH}_x$ in this work is approximately 21 % to 29 % [7]. In Experiment 1, with increasing Al content, the hydrogen content and hydrides significantly decreased. However, the number of cracks increased. It can be speculated that the solid-solution strengthening effect of Al reduces the accommodated deformation capacity of $\alpha\text{-Ti}$ matrix, leading to an increase in cracks.

The crack morphology in Ti-xAl alloys was further analyzed at high magnification (Fig. 10e-h). In Fig. 10e, cracks propagate along the intergranular hydrides, which is most prevalent in the Ti-2Al alloy. In Fig. 10f and g, the intergranular cracks deflect into transgranular cracks,

a move that was most prevalent in the Ti-4Al and Ti-6Al alloys. As for the Ti-8Al alloy, in Fig. 10h, the cracks extend at a nearly constant angle to the GBs, presenting a fishbone-like morphology. In this present study, a fishbone-like crack is defined as a characteristic microstructure consisting of at least three parallel-aligned transgranular cracks nucleated adjacent to the same hydride. The number of cracks in Ti-xAl alloys was then statistically analyzed. For each Al content, twenty non-overlapping regions (0.24 mm^2 each) were analyzed. This specific area was selected to ensure sufficient resolution for clear crack morphology identification. During statistical evaluation, regions near specimen edges were deliberately excluded to prevent the inclusion of stress concentration-induced cracks. This methodology ensured thorough crack detection while maintaining statistically reliable comparisons across alloy systems. As the Al content increases from 2 to 4 wt%, the number of transgranular cracks slightly increases from 50 to 248, while the proportion of intergranular cracks decreased. When the Al content ranges from 4 to 6 wt%, the number of transgranular cracks increases significantly from 248 to 653. In the Ti-8Al alloy, approximately 61 groups of fishbone cracks appear.

4. Discussions

4.1. The hindrance effect of Al on hydride nucleation

The solution energy and interaction energy of H occupying different positions near Al were calculated, as shown in Fig. 11. The solution energy corresponds to the energy barrier for hydrogen atoms to incorporate into the alloy lattice, where a lower value indicates a more favorable and stable solid solution. The interaction energy denotes the

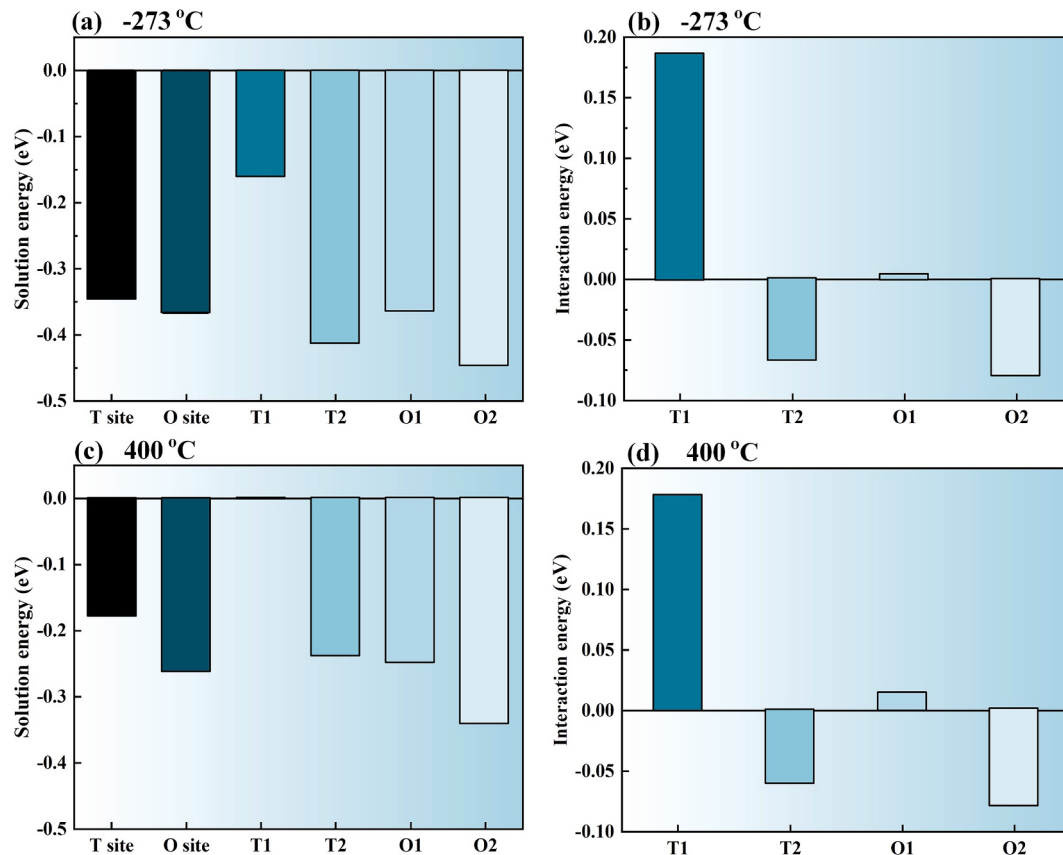


Fig. 11. Solution energies of H atoms in different interstitial sites of α -Ti at (a) -273 $^{\circ}\text{C}$ and (c) 400 $^{\circ}\text{C}$, respectively; interaction energies between Al atoms and H atoms in different interstitial sites at (b) -273 $^{\circ}\text{C}$ and (d) 400 $^{\circ}\text{C}$.

mutual forces between atoms, where positive and negative values respectively indicate repulsion and attraction. The T site and O site represent the tetrahedral interstitial sites and octahedral interstitial sites occupied by H atoms, respectively. T1 and T2 represent the positions where H atoms occupy the nearest neighbor and the next-nearest neighbor tetrahedral interstitial sites near Al atoms. The same applies to the O1 and O2 sites.

Fig. 11a and b illustrate the solution energy and interaction energy of H atoms at -273 $^{\circ}\text{C}$, respectively. Fig. 11a shows that the solution energy of H atoms dissolved in Ti alloy at all the interstitial sites is negative, indicating that hydrogen dissolution in Ti alloys is energetically favorable, especially at the O2 site. As shown in Fig. 11b, the interaction energy at the T1 and O1 positions is positive, while it is negative at the T2 and O2. Thus, Al and H atoms are mutually exclusive at the T1 and O1 positions, while they are attracted at the T2 and O2 positions. Fig. 11c and d depict the solution energy and interaction energy of H atoms at 400 $^{\circ}\text{C}$, showing results consistent with those in Fig. 11a and b at -273 $^{\circ}\text{C}$. The influence of temperature on the above energies is weak. Previous research shows that the tetrahedral site occupation of H in α -Ti is unstable, and solute H atoms mainly occupy the octahedral interstices [34]. Indeed, hydrogen dissolution at the O2 site is the most energetically favorable. The strong attraction of Al to H atoms at the O2 site hinders the formation of Ti-H bonds, thereby inhibiting the nucleation of hydrides.

The effect of Al on hydrides was also analyzed through the calculation of misfit strains induced by the α -Ti to TiH_x phase transformation. The c and a lattice parameters of the α -Ti unit cell at different Al contents were calculated from the peak positions in Fig. 1b, while the a parameter of δ - TiH_x was obtained from Fig. 5. Based on these data, the lattice distortion associated with hydride precipitation at varying Al contents was determined. The volume calculation formula for the close-packed

Table 3

Volume expansion associated with the precipitation of TiH_x in $\text{Ti}-x\text{Al}$ alloys with varying Al content.

Alloys	a_{α}	c_{α}	a_{δ}	V_{α}	V_{δ}	$(V_{\delta}-V_{\alpha})/V_{\alpha}$
Ti-2Al	0.2942	0.4681	0.4396	0.01754	0.0212	20.8 %
Ti-6Al	0.2929	0.4675	0.4394	0.01737	0.0212	21.8 %

hexagonal unit cell and the hydrides are given by $\sqrt{3}a_{\alpha}^2c_{\alpha}/4$ and $a_{\delta}^3/4$, respectively. It is observed that the volume expansion for hydride transformation increases as the Al content increases (Table 3). Moreover, studies have shown that the formation of different hydrides (γ and δ) is associated with prismatic, basal slip, atoms shuffle and Shockley dislocation in the matrix [35,36]. Calculated activation energies reveal pronounced hardening caused by Al addition for both slip systems [37,38]. Thus, the addition of Al suppresses hydride formation in titanium alloys.

4.2. The hydride OR affected by Al and H content

At low hydrogen concentration (about 0.1 wt%), hydrides prefer to follow OR2 in Ti-2Al and Ti-6Al (Fig. 8). In Ti-8Al, OR1 hydrides with numerous {111} stacking fault and twins are formed. The OR2 hydride transformation has a smaller strain misfit than OR1, leading to easier hydride nucleation. Prismatic and basal dislocations are attributed to the originating of OR1 and OR2 hydride transformation, respectively [36,39]. For Ti, a prismatic stacking fault has the lowest energy and corresponds to higher mobility of the dislocation core [40]. With increasing Al content, the interaction between Al atoms and H induces localized lattice distortion in the hydrides (Fig. 8f). High Al content

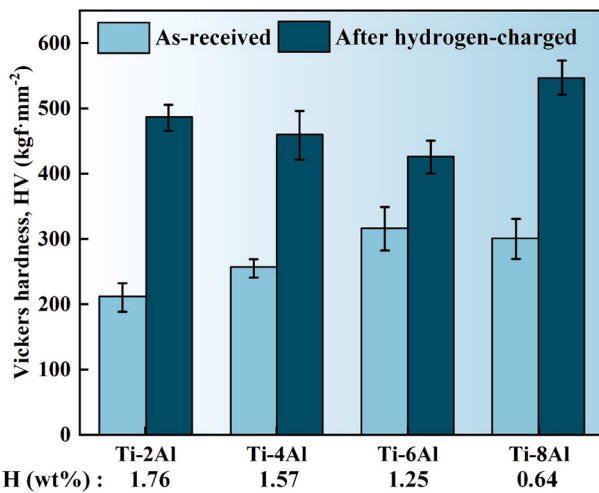


Fig. 12. The Vickers hardness of Ti-xAl alloys before and after hydrogen charging.

enhances the strength of the α -Ti matrix through solid solution strengthening, restricting the plastic deformation capability of the matrix surrounding the hydrides. Consequently, stress accommodation within the hydrides occurs primarily through twinning and stacking faults, leading to significantly increased defect density.

When the hydrogen content is higher than 0.5 wt%, only OR1 hydrides were observed, as shown in Fig. 7. Severe lattice distortion produced by massive hydride transformation needs to be accommodated by corresponding plastic deformation. Compared to OR2 transformation, the lattice distortion of OR1 hydride transformation can be better accommodated by prismatic dislocations.

4.3. Hydrogen-induced cracking with Al content

The hydrogen embrittlement mechanism was further investigated through Vickers hardness measurements of Ti-xAl ($x = 2, 4, 6, 8$ wt%) alloys before and after hydrogen charging (Fig. 12). The results

demonstrate that in Ti-2Al, Ti-4Al, and Ti-6Al alloys, increasing Al content prior to hydrogen charging enhanced matrix hardness. Since harder matrices are more susceptible to hydrogen embrittlement [41], hydrogen charging led to increased crack formation. With increasing Al content, the post-charging hardness declines, which is likely caused by either reduced hydrogen absorption or promoted crack initiation.

In contrast, Ti-8Al exhibited the lowest hydrogen absorption but significant hardness enhancement after charging (Fig. 12). As shown in Fig. 13a, no α_2 phase was observed in uncharged Ti-8Al alloy, whereas hydrogen charging induced α_2 precipitation (Fig. 13b). This phenomenon results from Al redistribution during hydrogen charging. Consequently, the substantial hardness increases in charged Ti-8Al is primarily caused by α_2 phase precipitation.

The nucleation of hydrogen-induced cracks at GBs, as depicted in Fig. 14a, is consistent with the findings of Kim et al [26]. Hydride sites exhibit higher dislocation densities, making them prone to defect-induced crack formation. The conditions of hydrogenation in a sealed tube maintain the alloy in an H_2 atmosphere. H_2 tends to accumulate at defect sites, leading to the development of hydrogen pressure within cracks (Fig. 14b). The hydrogen pressure acts as a force approximately aligned with the major axis of the ellipse [42]. Simultaneously, solute hydrogen atoms may accumulate at the crack tip, resulting in the formation of a plastic zone at the crack tip [42,43], as illustrated in Fig. 14b. The solid-solution strengthening effect of Al can diminish the plastic zone. When the plastic zone is substantial, cracks tend to extend along the tougher hydride phase within the plastic zone. Al is depleted in hydrides and enriched in the α -Ti matrix (Fig. 14c) [44]. Thus, with increasing Al content, Al atoms on both sides of the hydride compress the height of the plastic zone (l). Meanwhile, the height-to-width ratio (l/r) of the plastic zone is reduced, as shown in Fig. 14d. In most cases, cracks are more likely to propagate along the shorter axis of the plastic zone. When the Al content increases, the height of the plastic zone becomes smaller than its width, leading to the formation of transgranular and fishbone cracks.

5. Conclusions

The influence of Al content on the hydrogen behavior of Ti-xAl ($x =$

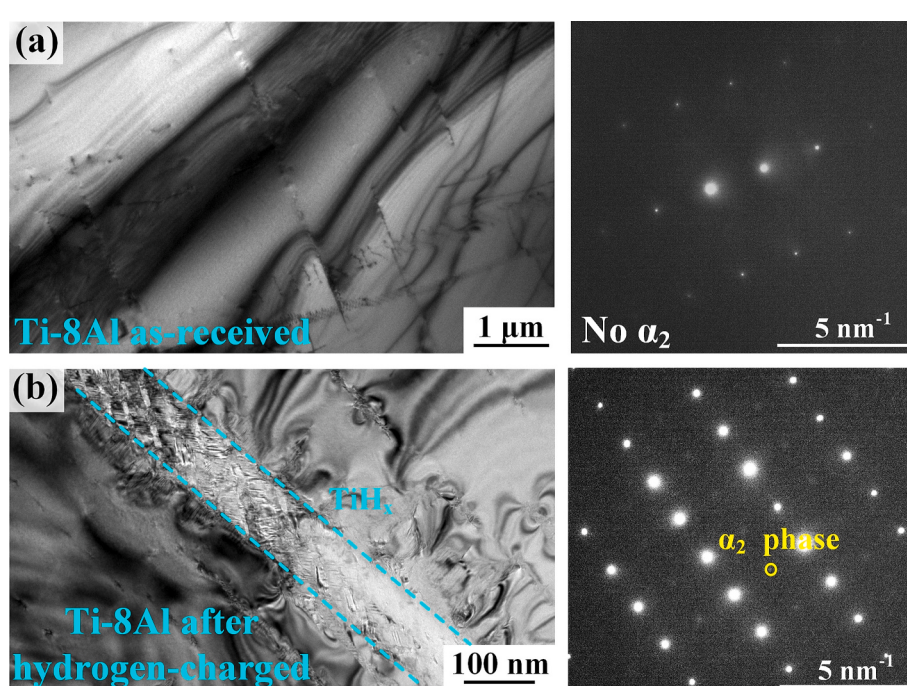


Fig. 13. TEM morphology of Ti-8Al alloy (a) before and (b) after hydrogen charging.

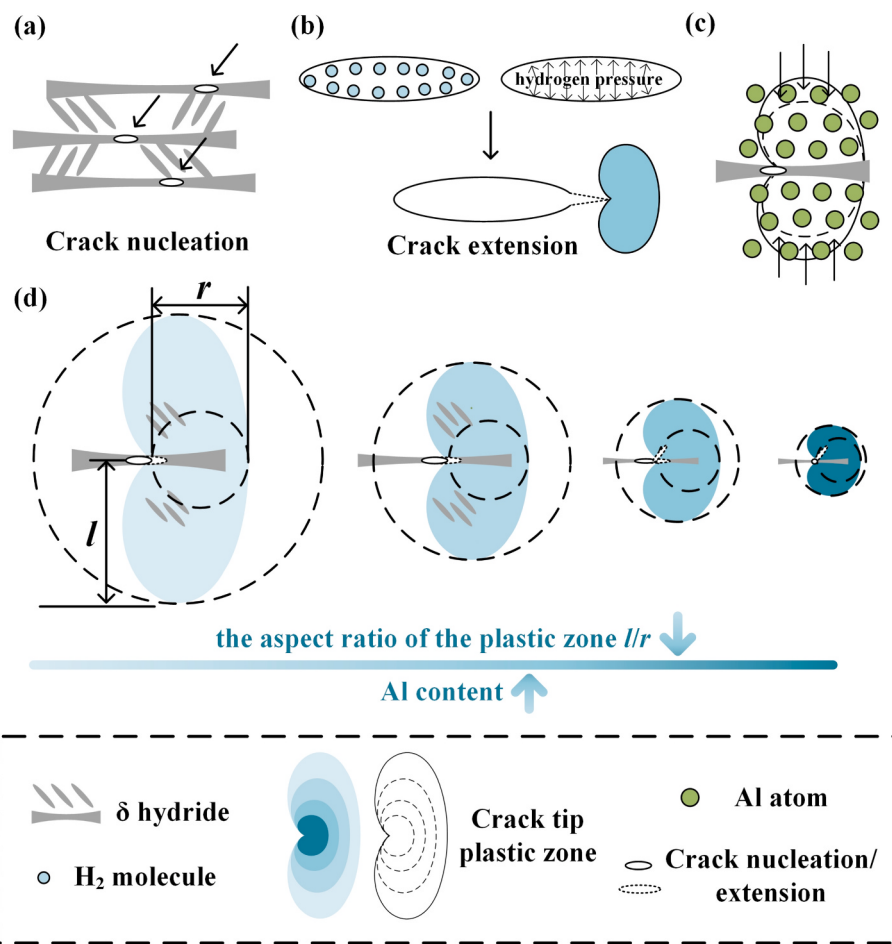


Fig. 14. Schematic diagram illustrating the process of hydrogen-induced crack in Ti-xAl alloys: (a) crack nucleation, (b) crack extension, and (c), (d) the influence of Al on the crack tip plastic zone.

2, 4, 6, 8 wt%) alloys was systematically investigated. The addition of Al to Ti-xAl alloys affects several key aspects of hydrogen behavior, including hydrogen absorption, diffusion, hydride transformation, and hydrogen-induced cracking. The primary conclusions of this study can be summarized as follows:

1. The addition of Al can reduce both the hydrogen absorption capacity and hydrogen diffusion rate of Ti-xAl alloys. The strong attraction of Al to H atoms in the octahedral interstitial sites hinders the formation of Ti-H bonds, thereby suppressing hydride nucleation. The larger lattice distortion associated with hydride transformation in Ti-xAl alloys with higher Al content is another reason for the inhibition of hydride precipitation.
2. With increasing hydrogen concentration, the dominant OR in Ti-xAl alloys changes from OR2 to OR1. At lower hydrogen content (about 0.1 wt%), hydride nucleation is accompanied by numerous {111} stacking faults or twins. At higher hydrogen contents (greater than 0.5 wt%), all hydrides exhibit OR1 with the α -Ti matrix. The variant with the minimum deviation between the hydride interface and the α lamella boundaries is preferentially selected.
3. The increase of Al content reduces the strain accommodation capacity, leading to more hydrogen-induced cracks. Compared with the intergranular cracks, the transgranular cracks are promoted significantly by increasing Al content. The interplay between Al and hydrides modifies the aspect ratio of the crack tip plastic zone and alters the mode of crack propagation.

CRediT authorship contribution statement

Hanbo Weng: Writing – original draft, Software, Methodology, Investigation, Formal analysis, Data curation, Conceptualization. **Qian Wang:** Writing – review & editing, Supervision, Software, Investigation, Funding acquisition, Conceptualization. **Linzhi Han:** Writing – review & editing, Software, Methodology. **Yandi Jia:** Writing – review & editing, Investigation, Data curation. **Shuo Cao:** Writing – review & editing, Conceptualization. **Yingjie Ma:** Writing – review & editing, Supervision, Software, Funding acquisition, Conceptualization. **Daokui Xu:** Writing – review & editing, Conceptualization. **Sensen Huang:** Writing – review & editing. **Min Qi:** Writing – review & editing, Conceptualization. **Qingmiao Hu:** Writing – review & editing, Conceptualization. **Jianke Qiu:** Writing – review & editing, Jiafeng Lei: Writing – review & editing, Conceptualization. **Rui Yang:** Writing – review & editing, Conceptualization.

Declaration of competing interest

The authors declare that they have no known competing financial interests or personal relationships that could have appeared to influence the work reported in this paper.

Acknowledgments

This work is supported by Natural Science Foundation of China (52401177, 52321001, U2106215), National Key Research and Development Program of China (2021YFC2801801), Special Research

Assistant Project of Chinese Academy of Sciences in 2022, Postdoctoral Science Foundation of China (2022M723213), Liaoning Provincial Natural Science Foundation of China (2023-BS-018).

Data availability

The raw/processed data required to reproduce these findings cannot be shared at this time as the data also forms part of an ongoing study.

References

- [1] D. Banerjee, J.C. Williams, Perspectives on titanium science and technology, *Acta Mater.* 61 (3) (2013) 844–879.
- [2] N. Derimow, J.T. Benzing, H. Joress, A. McDannald, P. Lu, F.W. DelRio, N. Moser, M.J. Connolly, A.I. Saville, O.L. Kafka, C. Beamer, R. Fishel, S. Sarker, C. Hadley, N. Hrabe, Microstructure and mechanical properties of laser powder bed fusion Ti-6Al-4V after HIP treatments with varied temperatures and cooling rates, *Mater. Des.* 247 (2024).
- [3] K.A. Abdesselam, S. Gaudet, S. Van Petegem, V. Honkimäki, S. Hallais, L. Cornet, M. Vallet, M.V. Upadhyay, Altering microstructure and enhancing mechanical properties during direct energy deposition of Ti-6Al-4V via in-process laser heat treatments, *Mater. Des.* 254 (2025).
- [4] H. Tobe, Y. Matsuki, S. Takeuchi, E. Sato, Deployable rocket nozzle utilizing superelastic titanium alloy sheet, *Mater. Trans.* 61 (1) (2020) 68–71.
- [5] L. Wang, C. Ye, C. Sun, S. Feng, X. Xie, Y. Gao, K. Zhao, Y. Li, Z. Wan, Experimental investigation on compressive dwell fatigue behavior of titanium alloy pressure hull for deep-sea manned submersibles, *Ocean Eng.* 303 (2024).
- [6] I.M.D.S. Shei, Robertson, H.K. Birnbaum, Hydrogen embrittlement of α titanium: in situ TEM studies, *Acta Metall.* 36 (1988) 111–124.
- [7] M.K.H. Numakura, Hydride precipitation in titanium, *Acta Mater.* 32 (10) (1984) 1799–1807.
- [8] E. Conforto, I. Guillot, X. Feaugas, Solute hydrogen and hydride phase implications on the plasticity of zirconium and titanium alloys: a review and some recent advances, *Philos. Trans. Royal Soc. A: Math. Phys. Eng. Sci.* 375 (2098) (2017).
- [9] G.K. Padhy, V. Ramasubbu, N. Parvathavarthini, C.S. Wu, S.K. Albert, Influence of temperature and alloying on the apparent diffusivity of hydrogen in high strength steel, *Int. J. Hydrogen Energy* 40 (20) (2015) 6714–6725.
- [10] T. Omura, H. Matsumoto, T. Hasegawa, Y. Miyakoshi, Effects of alloying elements on hydrogen entry to low alloy steels under a cyclic corrosion condition, *ISIJ Int.* 56 (3) (2016) 385–391.
- [11] T. Michler, J. Naumann, E. Sattler, Influence of copper as an alloying element on hydrogen environment embrittlement of austenitic stainless steel, *Int. J. Hydrogen Energy* 37 (17) (2012) 12765–12770.
- [12] J. Yi, X. Zhuang, J. He, M. He, W. Liu, S. Wang, Effect of Mo doping on the gaseous hydrogen embrittlement of a CoCrNi medium-entropy alloy, *Corros. Sci.* 189 (2021).
- [13] Q. Wang, H. Weng, T. Zhang, S. Huang, M. Qi, Y. Ma, C. Schuman, J.-S. Lecomte, D. Xu, J. Lei, R. Yang, Phase transformations induced by thermo hydrogen treatment in Ti-15 at.% Fe and Ti-15 at.% Cr alloys, *Acta Materialia* (2025).
- [14] Q. Wang, X. Liu, T. Zhu, F. Ye, M. Wan, P. Zhang, Y. Song, C. Huang, R. Ma, X. Ren, R. Yu, B. Wang, X. Cao, Mechanism of hydrogen-induced defects and cracking in Ti and Ti-Mo alloy, *Int. J. Hydrogen Energy* 48 (15) (2023) 5801–5809.
- [15] C.C. Liu, L.M. Zhang, Z. Liu, A.L. Ma, Z.X. Liu, Y.G. Zheng, Exploring the impact of Al alloying on microstructure and hot nitric acid corrosion resistance of Ti-xAl ($x=0, 1, 2, 3, 4, 5$) alloys, *Corros. Sci.* 232 (2024).
- [16] M.I. Lupo, A. Politi, G. Vigna, Hydrides in α -Ti: characterization and effect of applied external stresses, *Acta Mater.* 53 (19) (2005) 4987–4996.
- [17] E. Conforto, D. Caillard, A fast method for determining favourable orientation relationships and interface planes: application to titanium–titanium hydrides transformations, *Acta Mater.* 55 (3) (2007) 785–798.
- [18] F.X. Conforto, Hydrides formation and dissolution processes in zirconium alloys: crystallographic orientation relationships and stability after temperature cycling, *Proc. PTM* (2015) 231–238.
- [19] E. Conforto, S. Cohendoz, C. Berziou, P. Girault, X. Feaugas, Formation and dissolution of hydride precipitates in zirconium alloys: crystallographic orientation relationships and stability after temperature cycling, *Mater. Sci. Forum* 879 (2016) 2330–2335.
- [20] Q. Wang, S. Xu, J.-S. Lecomte, C. Schuman, L. Peltier, X. Shen, W. Song, Crystallographic orientation dependence of hydride precipitation in commercial pure titanium, *Acta Mater.* 183 (2020) 329–339.
- [21] F. Long, Y. Luo, N.N. Badr, O. Shiman, M. Topping, S.Y. Persaud, Z. Yao, L. K. Béland, M.R. Daymond, Identifying the true structure and origin of the water-quench induced hydride phase in Zr-2.5Nb alloy, *Acta Materialia* 221 (2021).
- [22] E. Tal-Gutelmacher, D. Eliezer, Hydrogen cracking in titanium-based alloys, *J. Alloy. Compd.* 404–406 (2005) 621–625.
- [23] Z.F.W.C.L. Briant, N. Chollocoop, Hydrogen embrittlement of commercial purity titanium, *Corros. Sci.* 44 (2002) 1875–1888.
- [24] Z. Pan, Y. Wei, Y. Fu, H. Luo, X. Li, Effect of electrochemical hydrogen charging on the mechanical property and corrosion behavior of Ti-3Mo alloy, *Corros. Sci.* 200 (2022).
- [25] S. Wang, D.K. Xu, Z.Q. Zhang, Y.J. Ma, Y.X. Qiao, Effect of electrochemical hydrogen charging on the mechanical behavior of a dual-phase Ti-4Al-2V-1Mo-1Fe (in wt.%) alloy, *Mater. Sci. Eng. A* (2021) 802.
- [26] J. Kim, E. Plancher, C.C. Tasan, Hydrogenation-induced lattice expansion and its effects on hydrogen diffusion and damage in Ti-6Al-4V, *Acta Mater.* 188 (2020) 686–696.
- [27] A. Behvar, M. Haghshenas, M.B. Djukic, Hydrogen embrittlement and hydrogen-induced crack initiation in additively manufactured metals: a critical review on mechanical and cyclic loading, *Int. J. Hydrogen Energy* 58 (2024) 1214–1239.
- [28] A. Alvarez, Hydrogen embrittlement of a metastable β -titanium alloy, *Acta Mater.* 52 (14) (2004) 4161–4175.
- [29] C.Q. Chen, S.X. Li, H. Zheng, L.B. Wang, K. Lu, An investigation on structure, deformation and fracture of hydrides in titanium with a large range of hydrogen contents, *Acta Mater.* 52 (12) (2004) 3697–3706.
- [30] J.F.G. Kresse, Efficiency of ab initio total energy calculations for metals and semiconductors using a plane-wave basis set, *Comput. Mater. Sci.* 6 (1996) 15–50.
- [31] G. Kresse, Efficient iterative schemes for ab initio total-energy calculations using a plane-wave basis set, *Phys. Rev. B* 54 (1996) 169–186.
- [32] K.B. John, P. Perdew, M. Ernzerhof, Generalized gradient approximation made simple, *Phys. Rev. Lett.* 77 (1996) 3865–3868.
- [33] J. Hu, X. Li, L. Vitos, S. Schönecker, Effects of Mg and Al doping on the desorption energetics and electronic structure of a Ti-V-Zr-Nb alloy hydride, *Acta Mater.* 277 (2024).
- [34] C.-M. Wang, S. Cao, F.-X. Yang, Y.-J. Ma, H. Su, A.-Q. Fu, S.-Z. Zhang, R. Yang, Q.-M. Hu, Insights into the formation of titanium hydrides from first principles calculations, *Acta Mater.* 272 (2024).
- [35] J. Li, X. Li, M. Sui, Formation mechanism of hydride precipitation in commercially pure titanium, *J. Mater. Sci. Technol.* 81 (2021) 108–116.
- [36] Q. Wang, S. Xu, Y. Zhao, J.-S. Lecomte, C. Schuman, Multi-dimensional morphology of hydride diffusion layer and associated sequential twinning in commercial pure titanium, *J. Mater. Sci. Technol.* 103 (2022) 105–112.
- [37] R.G.B.J.C. Williams, N.E. Paton, Deformation behavior of HCPTi-Al alloy single crystals, *Metall. Mater. Trans. A-Physical Metall. Mater. Sci.* 33 (2002) 837–850.
- [38] P. Kwasniak, S. Delannoy, F. Prima, E. Clouet, Competition between prismatic and basal slip in hexagonal titanium–aluminum alloys with short-range order, *Mater. Res. Lett.* 11 (6) (2023) 407–413.
- [39] X.-Y. Zhou, W. Lu, X. Peng, X. Zhuang, M. Wang, X.-S. Yang, S. Ye, H.-H. Wu, Dissecting the phase transformation mechanism of titanium hydride at atomic scale, *Acta Mater.* 288 (2025).
- [40] M. Ghazisaeidi, D.R. Trinkle, Core structure of a screw dislocation in Ti from density functional theory and classical potentials, *Acta Mater.* 60 (3) (2012) 1287–1292.
- [41] O.R. A., Hydrogen embrittlement of steels, *Annu. Rev. Mater. Sci.* 8 (1978) 327–357.
- [42] A. Traidia, M. Alfano, G. Lubineau, S. Duval, A. Sherik, An effective finite element model for the prediction of hydrogen induced cracking in steel pipelines, *Int. J. Hydrogen Energy* 37 (21) (2012) 16214–16230.
- [43] S. Cao, S. Zhu, C.V. Samuel Lim, X. Zhou, X. Chen, B.R.W. Hinton, R.R. Boyer, J. C. Williams, X. Wu, The mechanism of aqueous stress-corrosion cracking of $\alpha + \beta$ titanium alloys, *Corros. Sci.* 125 (2017) 29–39.
- [44] Y. Chang, A.J. Breen, Z. Tarzimoghadam, P. Kürnsteiner, H. Gardner, A. Ackerman, A. Radecka, P.A.J. Bagot, W. Lu, T. Li, E.A. Jägle, M. Herbig, I.T. Stephenson, M. P. Moody, D. Rugg, D. Dye, D. Ponge, D. Raabe, B. Gault, Characterizing solute hydrogen and hydrides in pure and alloyed titanium at the atomic scale, *Acta Mater.* 150 (2018) 273–280.